

# Electronic and magnetic ground states of $\{112\}$ grain boundary in graphene in the extended Hubbard model

Sishir Jana,<sup>1</sup> Dayasindhu Dey,<sup>2</sup> Manoranjan Kumar,<sup>3</sup> S. Ramasesha,<sup>4</sup> and Rajamani Raghunathan<sup>1</sup>

<sup>1</sup>*UGC-DAE Consortium for Scientific Research, DAVV Campus, Khandwa Road, Indore - 452001.\**

<sup>2</sup>*Department of Physics, School of Advanced Sciences, Vellore Institute of Technology (VIT), Chennai Campus, Chennai 600 127 Tamil Nadu, India*

<sup>3</sup>*S.N. Bose National Centre for Basic Sciences, Block-JD, Sector-III, Salt Lake, Kolkata - 700106.*

<sup>4</sup>*Solid State and Structural Chemistry Unit, Indian Institute of Science, Bangalore - 560012.*

(Dated: July 15, 2025)

We study the ground state phase diagram of the extended Hubbard model in a half-filled  $5/7$  skewed ladder, which is topologically equivalent to a  $\{112\}$  grain boundary in graphene and related systems. Using the mean-field method, we identify various electronic and magnetic phases in the  $U$ - $V$  plane, by calculating the site charge and spin densities. The electronic phases include partially charge-ordered metal or insulator, and fully charge-ordered insulator. The different magnetic phases of the model are non-magnet, spin density wave, spin split compensated ferrimagnet or partial antiferromagnet. Analysis of the electronic band structure reveals that the partially charge-ordered compensated ferrimagnetic phase exhibits spin polarisation, which can be quite interesting for spintronics applications. We also compute the polarisation as a function of  $U$  using the Berry phase formalism and show that the system exhibits multiferroicity with coexisting compensated ferrimagnetic spin order alongside electronic polarisations.

## I. Introduction

Modeling quantum phase transition (QPT) in low-dimensional systems is fundamentally significant, as it reveals novel electronic [1] and magnetic [2] ground states within the model parameter space. The quantum fluctuations in low-dimensional systems are confined and give rise to many interesting quantum phases in the ground state [3]. These fluctuations further determine the low temperature electronic [4, 5] and magnetic [6] behaviours of the system. Many of these quantum systems exhibit charge [7] or spin frustration [8] due to competing interactions, leading to several exotic quantum phases like the charge density wave (CDW) [9], spin density wave (SDW) [10], bond order wave (BOW) [11], spiral [12] or dimer order [13] etc. To model these quantum phases, extended Hubbard model [14] and various types of Heisenberg models have been employed on one-dimensional chains [15], triangular [16] and square ladders [17], as well as skewed ladder systems [18, 19].

Skewed ladder systems consist of two-leg ladders with slanted rung interactions between the legs. Among these, the  $5/7$  skewed ladder which is shown in the figure 1 is particularly interesting due to its resemblance to the structure of fused Azulenes and is also formed at the  $\{112\}$  grain boundary of graphene. Using the Pariser-Parr-Pople (PPP) model, Thomas et al. demonstrated that fused Azulene can function as a room-temperature organic multiferroic material [20]. Giri and coworkers have also applied the PPP model to investigate singlet fission in polycyclic aromatic hydrocarbons [21]. More

recently, Valentim et al. explored the magnetic phase diagram of the Hubbard model in a  $5/7$  ladder, revealing a system size ( $n$ )-dependent magnetic phase transition from a singlet ( $S = 0$ ) to higher spin ground states ( $S = 1, 2$ ) in the  $U$  vs.  $n$  phase space, which was first observed in the PPP model and the Heisenberg spin model by Thomas et al. [22].

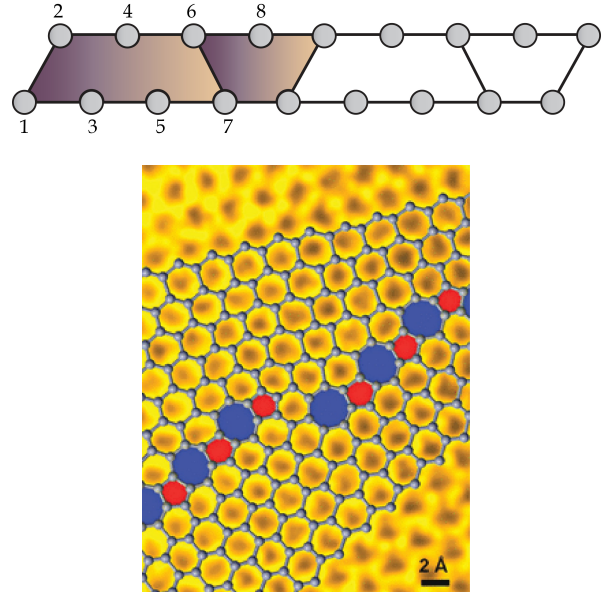


FIG. 1: (Top) Unit cell of a  $5/7$  skewed ladder system. (Bottom) Scanning transmission electron microscopy (STEM) image of  $\{112\}$  grain boundary reproduced with permission from [23]. Copyright 2011 ACS. The black spheres in the figure represent the carbon atoms.

\* Corresponding author: rajamani@csr.res.in

In addition to the electronic models, several studies

have explored the magnetic phases in the ground state of skewed ladders using Heisenberg spin-1/2 and spin-1 models. [18, 24]. Notably, systems such as 3/4, 3/5 and 5/7 skewed ladders exhibit a quantum phase transition (QPT) from non-magnetic to ferrimagnetic ground state. These QPT boundaries can be identified by analyzing the discontinuities in the entanglement entropy and sharp dips in the fidelity at the phase boundaries [25, 26]. Additionally, the spin-1/2 5/7 skewed ladder is also known to exhibit unusual plateaus at 1/4, 1/2 and 3/4 magnetizations [19]. Studies of the spin-1 5/7 skewed ladders have shown the presence of a vector chiral phase induced by the breaking of both reflection and parity symmetries in the ground state [18, 27].

Beyond model systems, skewed ladder structures are also interesting due to their similarity to grain boundaries (GBs) commonly found in two-dimensional materials like graphene and bulk materials such as silicon. Hsieh and coworkers, through 1/f noise studies on graphene GBs have demonstrated spontaneous time-reversal symmetry breaking, leading to ferromagnetism [28]. Investigations of various prevalent GBs in silicon have further revealed distinct electronic structures. Notably, the {112} GB, which closely resembles the 5/7 skewed ladder, exhibits a metallic ground state, whereas other GBs display a gaped nature [29]. These prior studies suggest that 5/7 skewed ladders could host a wide range of electronic and magnetic phases.

In order to understand the electronic properties of GBs, it is essential to study 5/7 skewed ladder using models like the extended Hubbard model. The presence of both on-site ( $U$ ) and inter-site ( $V$ ) Coulomb repulsions can host more exotic properties due to the competition between the charge and spin degrees of freedom. We therefore investigate here the emerging electronic and magnetic phases on a 5/7 skewed ladder system using an extended Hubbard model at half-filling.

In this work we analyze the extended Hubbard model using a mean-field approach. We construct the quantum phase diagram in the  $U$  vs.  $V$  parameter space, and also show that the phase diagram exhibits rich electronic and magnetic phases in the model parameter space including partially charge-ordered metal or insulator, fully charge-ordered insulator, spin density wave metal and spin split compensated ferrimagnet (SS CFiM). These phases are characterized using the site spin and charge densities as well as the electronic band structures. Finally, we present the results of our polarization calculations and conclude.

## II. Model and Method

The extended Hubbard model that describes a 5/7 skewed ladder system is given by,

$$\begin{aligned} \hat{\mathcal{H}}_{5/7} = & -t \sum_{i=0}^{n-1} \sum_{j=1}^8 \sum_{\sigma} \left( \hat{c}_{8i+j,\sigma}^{\dagger} \hat{c}_{8i+j+2,\sigma} + \text{h.c.} \right) \\ & -t \sum_{i=0}^{n-1} \sum_{\sigma} \left( \hat{c}_{8i+1,\sigma}^{\dagger} \hat{c}_{8i+2,\sigma} + \hat{c}_{8i+6,\sigma}^{\dagger} \hat{c}_{8i+7,\sigma} + \text{h.c.} \right) \\ & +U \sum_{i=0}^{n-1} \sum_{j=1}^8 \hat{n}_{8i+j,\uparrow} \hat{n}_{8i+j,\downarrow} \\ & +V \sum_{i=0}^{n-1} \sum_{j=1}^8 \hat{n}_{8i+j} \hat{n}_{8i+j+2} + V \sum_{i=0}^n \hat{n}_{8i+1} \hat{n}_{8i+2} \quad (1) \end{aligned}$$

where,  $i$  labels the unit cell,  $j$  represents the site within the unit cell and  $n$  represents the number of unit-cells. The operators  $\hat{c}_{i,\sigma}^{\dagger}$  and  $\hat{c}_{i,\sigma}$  are the creation and annihilation operators at site  $i$  with spin  $\sigma$  respectively,  $t$  is the hopping parameter, representing the kinetic energy of electrons hopping between neighboring sites. The parameter  $U$  is the on-site Coulomb repulsion term, accounting for the energy cost of two electrons occupying the same site,  $V$  is the inter-site Coulomb repulsion term, representing the repulsion energy for electrons on neighboring sites. The operator  $\hat{n}_{i,\sigma} = \hat{c}_{i,\sigma}^{\dagger} \hat{c}_{i,\sigma}$  is the number operator for electrons with spin  $\sigma$  at site  $i$ . The total electron number operator at site  $i$  is given by  $\hat{n}_i = \sum_{\sigma} \hat{n}_{i,\sigma}$ . In equation 1 the terms in the first two lines correspond to the leg and rung hopping, the third line accounts for the on-site Coulomb repulsion at site  $j$  and the inter-site Coulomb repulsions forms the last line.

The real-space Hamiltonian in the equation 1 can be transformed into the reciprocal or  $\mathbf{k}$  space ( $\hat{\mathcal{H}}_{\mathbf{k}}$ ) by doing a discrete Fourier transform of the creation and annihilation operators as shown in the equation 2.

$$\begin{aligned} \hat{c}_{i,\sigma}^{\dagger} &= \frac{1}{\sqrt{N}} \sum_{\mathbf{k}} e^{-i\mathbf{k}\cdot\mathbf{r}_i} \hat{c}_{\mathbf{k},\sigma}^{\dagger} \\ \hat{c}_{i,\sigma} &= \frac{1}{\sqrt{N}} \sum_{\mathbf{k}} e^{i\mathbf{k}\cdot\mathbf{r}_i} \hat{c}_{\mathbf{k},\sigma} \quad (2) \end{aligned}$$

where  $N$  is the number of atoms in the unit-cell. The  $\mathbf{k}$  space Hamiltonian,  $\hat{\mathcal{H}}_{\mathbf{k}}$  obeys the relation shown in the equation 3.

$$\begin{aligned} \hat{\mathcal{H}} &= \sum_{\mathbf{k}} \psi_{\mathbf{k}}^{\dagger} \hat{\mathcal{H}}_{\mathbf{k}} \psi_{\mathbf{k}} \\ \hat{\mathcal{H}}_{\mathbf{k}} &= \hat{\mathcal{H}}_{\mathbf{k}}^{\uparrow} \oplus \hat{\mathcal{H}}_{\mathbf{k}}^{\downarrow} \end{aligned}$$

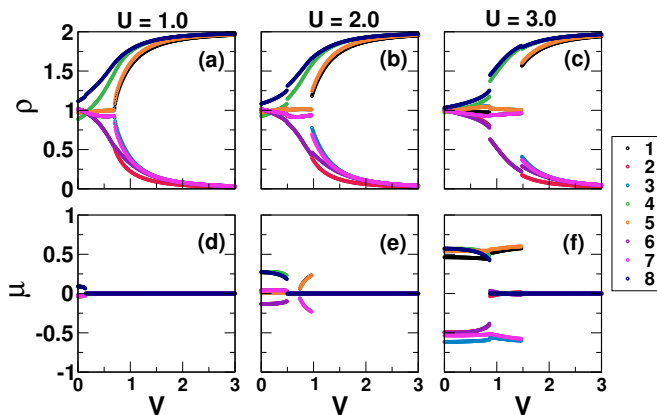


FIG. 2: Variation of site charge (a-c) and spin (d-f) densities as a function  $V$  for  $U=1.0, 2.0$  and  $3.0$ . There is a minor charge difference in charge densities of sites 4 and 8 (upper-leg) even at  $t=0$ . The CO transitions are continuous at lower- $U$  and discontinuous in the large  $U$  limit. The magnetic transitions are by and large discontinuous.

$$\text{and } \psi_{\mathbf{k}} = \begin{pmatrix} c_{1\mathbf{k}\uparrow} \\ c_{2\mathbf{k}\uparrow} \\ c_{3\mathbf{k}\uparrow} \\ c_{4\mathbf{k}\uparrow} \\ c_{5\mathbf{k}\uparrow} \\ c_{6\mathbf{k}\uparrow} \\ c_{7\mathbf{k}\uparrow} \\ c_{8\mathbf{k}\uparrow} \end{pmatrix} \otimes \begin{pmatrix} c_{1\mathbf{k}\downarrow} \\ c_{2\mathbf{k}\downarrow} \\ c_{3\mathbf{k}\downarrow} \\ c_{4\mathbf{k}\downarrow} \\ c_{5\mathbf{k}\downarrow} \\ c_{6\mathbf{k}\downarrow} \\ c_{7\mathbf{k}\downarrow} \\ c_{8\mathbf{k}\downarrow} \end{pmatrix} \quad (3)$$

The model is solved using a mean-field approach [30] in which the operator  $\hat{n}_i$  is written as the sum of its expectation value  $\langle \hat{n}_i \rangle$  and its fluctuation  $\Delta n_i$ ,  $\hat{n}_i \approx \langle \hat{n}_i \rangle + \Delta n_i$ . The system is initialised with suitable spin ( $\mu$ ) and charge densities ( $\rho$ ) on every site to represent a chosen electronic and magnetic state. The Hamiltonian matrix for the up- and the down-spin electrons is constructed in the  $\mathbf{k}$  space ( $\hat{\mathcal{H}}_{\mathbf{k}}^\sigma$ ) and the same is presented in the supporting information (SI) file. This Hamiltonian is diagonalised to obtain the eigenvalues and the corresponding eigenvectors. The  $\mu$  and  $\rho$  are then computed from the eigenvector, which form the inputs for the next iteration. The iterative process is repeated until a chosen convergence criterion on the charge density difference,  $\delta\rho = 10^{-5}$  is reached. In order to obtain the correct ground state, the system is also started with different initial electronic and magnetic configurations by altering the starting site charge and spin densities respectively. The energies of such configurations are compared to determine the electronic and magnetic ground states. The converged ground state wave functions are then used to calculate the band structure, density of states (DOS) as well as charge and spin densities as a function of  $U$  and  $V$  in order to characterize different phases. The value of

the hopping parameter ( $t$ ) in the Hamiltonian in equation 1 is kept fixed at 1 eV, which serves as the energy scale for the parameters  $U$  and  $V$ . The values of the model parameters  $U$  and  $V$  are varied in the range  $0-6t$  and  $0-3t$ .

### III. Results

#### A. Symmetry of the 5/7 Skewed Ladder

The unit cell of our 5/7 skewed ladder consists of eight sites, with each site possessing on an average one electron in one orbital. This corresponds to the half-filled skewed ladder. The sites are numbered such that the lower leg sites are odd numbered, and the upper leg has even numbered sites as shown in figure 1. The connectivities 1-2 and 6-7 form the rung bonds. This unit cell can be repeated along the  $-x$  and  $+x$  directions to obtain the entire ladder. The unit cell of our model has few inherent symmetries. These include (i) a mirror  $\sigma$  with its plane passing along sites 4 and 8, or a  $C_2$  symmetry element whose rotation axis passes through sites 4 and 8 (ii) a parity or spin-inversion symmetry  $\mathcal{P}$  which corresponds to inversion of the spin from  $+s$  to  $-s$  or vice-versa and (iii) a combination of the the first two symmetries  $\sigma$  and  $\mathcal{P}$ . Therefore, the symmetry elements of the ladder can be written as  $\{E, \sigma, \mathcal{P}, \sigma\mathcal{P}\}$ , where  $E$  is the identity operator. Action of these symmetry elements on different fermionic and bosonic operators for  $N = 8$  sites is shown in the table I.

#### B. Charge density

First we discuss the site charge density  $\rho$  of the model for different  $V$ , which is shown in the figure 2 a-c. It would be instructive to understand the  $t = 0$  behaviour. A large value of  $U$  will stabilise those states which have single occupancy of the orbitals. On the other hand the parameter  $V$  adds an energy cost when the orbitals on the neighbouring sites are both occupied, thereby favouring double occupancy on the alternate sites. Therefore, the  $U$  and  $V$  parameters stabilise those states with singly or doubly occupied orbitals respectively. In this limit the charge ordering will occur whenever  $V \geq U/2$ . Now we turn our attention to the  $t \neq 0$  behaviour. The 5/7 ladder hosts mirror symmetry  $\sigma$ , the plane of which passes through sites 4 and 8, and perpendicular to the plane of the ladder. Hence, the charge densities of the sites 1 and 7, 3 and 5 as well 2 and 6 are the same in those phases where  $\sigma$  or  $\sigma\mathcal{P}$  symmetry is conserved. For non-zero but very small hopping parameter, we notice that there is a subtle charge difference between the sites 4 and 8 even for  $V < U/2$ . Therefore we calculated  $\rho$  in the  $t \rightarrow 0$  limit ( $t=0.001$ ), in which case there is no charge difference between these two sites for  $V < U/2$ . Also, when we turn off the hopping parameter for the rung bonds,

Operator	$E$	$\sigma$	$\mathcal{P}$	$\sigma\mathcal{P}$
$S_i^x$	$S_i^x$	$\begin{cases} S_{N-i}^x & \text{if } i \neq N, N/2 \\ S_i^x & \text{if } i = N, N/2 \end{cases}$	$-S_i^x$	$\begin{cases} -S_{N-i}^x & \text{if } i \neq N, N/2 \\ -S_i^x & \text{if } i = N, N/2 \end{cases}$
$S_i^y$	$S_i^y$	$\begin{cases} S_{N-i}^y & \text{if } i \neq N, N/2 \\ S_i^y & \text{if } i = N, N/2 \end{cases}$	$S_i^y$	$\begin{cases} S_{N-i}^y & \text{if } i \neq N, N/2 \\ S_i^y & \text{if } i = N, N/2 \end{cases}$
$S_i^z$	$S_i^z$	$\begin{cases} S_{N-i}^z & \text{if } i \neq N, N/2 \\ S_i^z & \text{if } i = N, N/2 \end{cases}$	$-S_i^z$	$\begin{cases} -S_{N-i}^z & \text{if } i \neq N, N/2 \\ -S_i^z & \text{if } i = N, N/2 \end{cases}$
$c_{i,\uparrow}$	$c_{i,\uparrow}$	$\begin{cases} c_{N-i,\uparrow} & \text{if } i \neq N, N/2 \\ c_{i,\uparrow} & \text{if } i = N, N/2 \end{cases}$	$c_{i,\downarrow}$	$\begin{cases} c_{N-i,\downarrow} & \text{if } i \neq N, N/2 \\ c_{i,\downarrow} & \text{if } i = N, N/2 \end{cases}$
$c_{i,\downarrow}$	$c_{i,\downarrow}$	$\begin{cases} c_{N-i,\downarrow} & \text{if } i \neq N, N/2 \\ c_{i,\downarrow} & \text{if } i = N, N/2 \end{cases}$	$-c_{i,\uparrow}$	$\begin{cases} -c_{N-i,\uparrow} & \text{if } i \neq N, N/2 \\ -c_{i,\uparrow} & \text{if } i = N, N/2 \end{cases}$

TABLE I: Transformation properties of various spin and electronic operators under the symmetry operations,  $E$ ,  $\sigma$ ,  $\mathcal{P}$  and  $\sigma\mathcal{P}$ .

keeping the  $t$  of leg bonds non-zero, the site charge differences are negligible. Hence we conclude that the charge difference between the sites 4 and 8 in the  $t \neq 0$  limit originates from the rung bonds. We further notice that the charge difference is large when the value of  $U$  is less. The charge densities of different sites in the upper and lower legs begin to bifurcate at higher values of  $V$  leading to charge-order (CO). Moreover, the onset of bifurcation in the upper leg occurs at a lower value of  $V$  compared to the lower leg for a  $U$  value. For any given  $U$  value, when the inter-site repulsion,  $V$  is weak, the upper leg shows charge-ordering while the lower leg shows uniform charge density. We refer to this as the partially charge-ordered (PCO) phase. For instance, when  $U = 1$  and  $V = 0.25$ ,  $\rho$  of sites 4 and 8 start increasing with  $V$  whereas the charge density of sites 2 and 6 decrease, however the charge density of sites in the lower leg remain uniform and close to 1. A similar trend is observed for higher  $U$  values also. This could be due to the difference in the topology of the upper and lower leg. The upper leg has three sites between two rungs while the lower leg has either two or four sites between any two rungs. The odd number of sites between rung bonds leads to frustration in the local rings and hence delocalisation is reduced therefore the system prefers a charge ordered state. For large values of  $V$  we notice that both the upper and lower legs are charge-ordered, which we refer as the fully charge-ordered (FCO) phase. The FCO phase is doubly degenerate with charge configurations FCO1 and FCO2, due to the presence of mirror symmetry.

### C. Magnetic moment

The magnetic moment of site  $i$  ( $\mu_i = (n_{i\uparrow} - n_{i\downarrow})$ ) computed as a function of  $V$  at different  $U$  values is presented in figure 2 d-f. The plot reveals that for small  $U$ , the magnetic moment of all the eight sites are negligibly small, corresponding to a non-magnetic (NM) state. When  $U$  is increased to 2.0, the sites on the upper leg show non-zero

moments while the sites on the lower leg have nearly zero moment. This can again be attributed to the magnetic frustration in the upper leg. In the lower leg the spin on initial site almost determines the spin on other sites. Furthermore, the spin at the initial site of the leg can be up or down, leading to zero mean spin density. We further notice that at  $V = 0$ , the spin magnetic moments of sites 4 and 8 are large positive (about  $+0.25 \mu_B$ ) and those of sites 2 and 6 are relatively smaller and also negative (about  $-0.15 \mu_B$ ). This means that the upper leg shows SDW, while the lower leg is non-magnetic. When  $V$  is increased gradually, the SDW order of the upper leg ceases and the entire ladder develops a non-magnetic (NM) phase. Upon further increasing  $V$  an antiferromagnetic order develops in the lower leg, while the upper leg still remains non-magnetic, which we call the partially antiferromagnetic (PAFM) phase. Finally the antiferromagnetic order in the lower leg also melts into a NM phase at high  $V$  values.

For  $U > 3$  and  $0 \leq V \leq 0.9$ , we observe anti-parallel alignment of magnetic moments in both the legs, with moment value close to  $0.5 \mu_B$ . The calculated spin densities in this region reveal that the site moments are opposite in direction but not equal in magnitude, like the ferrimagnets. However, the total magnetic moment of the unit-cell is zero similar to the conventional antiferromagnets. This type of magnetic ordering is unique in the sense that this magnetic phase has the characteristics of both ferrimagnets and antiferromagnets. We will later show that the electronic structure of this phase shows spin polarisation of the up- and down-spin bands. Therefore, we designate this phase as the partially charge-ordered, spin split (SS) compensated ferrimagnet (CFiM), PCO + SS CFiM. The magnetic ground state of this phase consists of two unique magnetic configurations, CFiM1 and CFiM2 as shown in the figure 3. Each of these magnetic configurations are doubly degenerate, thus making the ground state to be four-fold degenerate. Moreover, the CFiM1 and CFiM2 configurations are related by a combination of  $\sigma$  and  $\mathcal{P}$  symmetry. The other

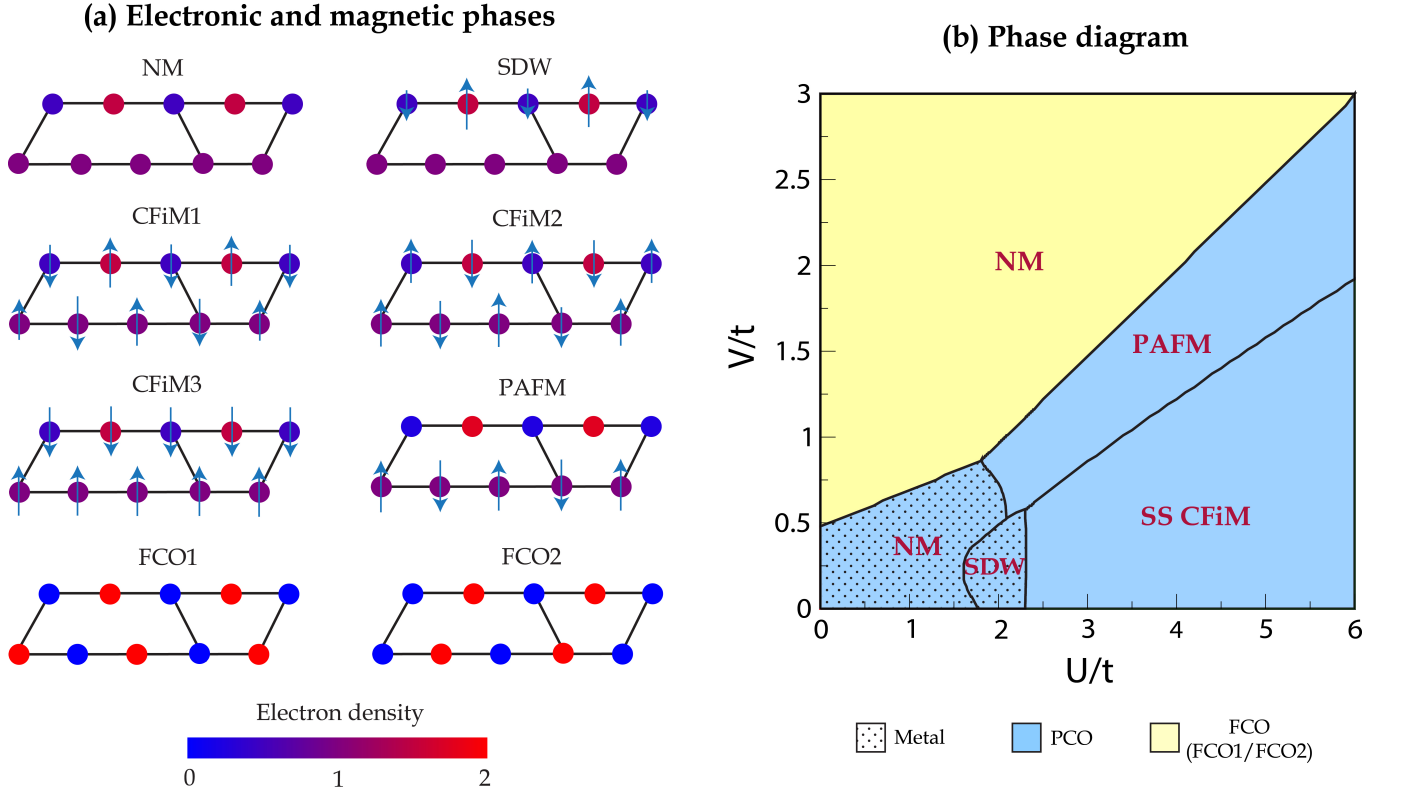


FIG. 3: (a) Schematic of various electronic and magnetic phases of the model. The color scale from blue through red represent the value of charge density  $\rho$  on each site. A perfect blue/red color corresponds to  $\rho = 0$  (empty) or 2 (doubly occupied) respectively. The up- and down-spins are represented by the direction of the arrows and the length of the arrow represents the magnitude. (b) Phase diagram of the 5/7 ladder the  $U$  vs.  $V$  plane. The blue shaded regions are partially charge-ordered phases and the yellow region corresponds to the fully CO (FCO) phase. The dotted regions are the metallic phases and the un-dotted regions are gaped phases. The various phases seen in the phase diagram are the PCO+NM (Blue+dot), PCO+SDW (Blue+dot), PCO+SS CFiM (Blue), PCO+PAFM (Blue) and FCO+NM (yellow).

possible spin configuration, CFiM3 is higher in energy. This can be easily understood from the energies of the singlet and triplet pairs in the localisation limit, which are respectively  $-3/4J$  and  $1/4J$ . For the CFiM1 and CFiM2 phases, out of the total eight bonds, seven are antiferromagnetically coupled while one bond is ferromagnetic, yielding a total energy of  $-5J$ . However, in the CFiM3 phase two bonds are antiferromagnetic and six bonds are ferromagnetic, with total energy  $0J$ . Hence, the CFiM1 and CFiM2 phases are degenerate and lower in energy than the CFiM3 phase.

Increasing  $V$  at large  $U$  leads to PCO + SS CFiM to PCO + PAFM phase transition in which the upper leg becomes non-magnetic due to the onset of charge-order in that leg, while the lower leg retains the antiferromagnetic order. Upon further increasing  $V$  the system transforms to a NM phase due to the charge-ordering in both the legs. We also observe that for a given  $V$ , the magnetic moment increases with increasing  $U$  value due to the enhanced localisation. The results of the charge and spin

densities of the model can be combined to identify different phases of the system in the model parameter space of  $U$  and  $V$  namely PCO+NM, PCO+SDW, PCO+SS CFiM, PCO+PAFM and FCO+NM, as depicted in the figure 3.

#### D. Electronic Structure

We now discuss the electronic band structures of the different phases of the model as presented in figure 4. The bands corresponding to  $\uparrow$  and  $\downarrow$  spin are plotted as red-continuous and blue-dashed lines respectively. The electronic band structures of different phases are obtained in the middle of the phase, far enough from the phase boundary. The unit cell of the 5/7 skewed ladder consists of eight sites and the electronic band structure exhibits eight bands each in up- and down-spin channels. We observe that the phases corresponding to low  $U$  and  $V$  values namely PCO+NM and PCO+SDW are metallic in nature, depicted as dotted region in the phase dia-



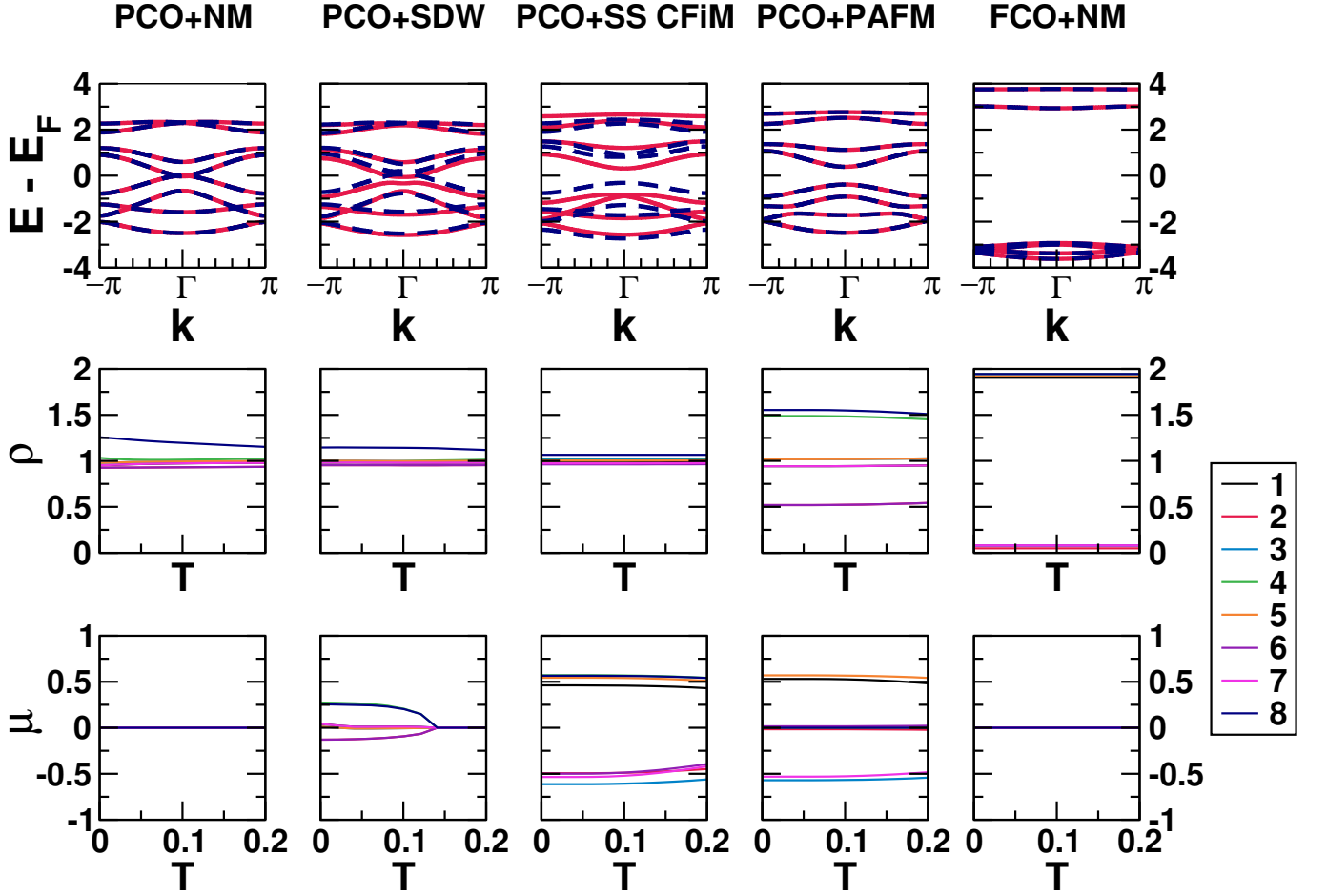


FIG. 4: (Top row) Band structure in PCO+NM, PCO+SDW, PCO+SS CFiM, PCO+PAFM and FCO+NM phases of the model from  $k = -\pi$  to  $+\pi$ . The Fermi level is fixed at 0 eV. The up- and down-spin channels are plotted separately in red (continuous) and blue (dashed) lines. (Middle row) Charge density,  $\rho$  as a function of temperature in the range  $0-2t$ . (Bottom row) Temperature (in units of  $t/k_B$ ) dependence of spin density  $\mu$  in different phases of the model.

gram of figure 3(c). The electronic bands of these two phases are very similar, except for the spin polarization between the bands corresponding to the up- and the down-spin channels in the SDW phase. The FCO+NM, PCO+PAFM and PCO+SS CFiM phases show a gaped behaviour. The electronic band gap of the FCO phase is the largest. The FCO+NM and PCO+PAFM phases do not show any spin polarization, but the PCO+SS CFiM phase shows considerable spin polarization. The presence of spin polarization in PCO+SS CFiM phase is quite interesting as the electronic bands of antiferromagnets are generally spin degenerate. However, momentum dependent spin polarization has been reported recently in certain unconventional antiferromagnets known as the altermagnets [31]. This is because, in altermagnets the neighbouring magnetic ions are related by spin-inversion plus an additional real space rotation symmetry [32]. On the contrary, in conventional antiferromagnets, the neighbouring sites are related by spin-inversion plus a real space translation symmetry [32]. For this reason,

conventional AFMs do not show spin polarisation. But in case of our 5/7 skewed ladder, the spin polarization results from the unequal and opposite spin densities on different sites, while the total spin density of all the sites of the unit cell is zero. This magnetic ordering is different from ferrimagnetic ordering in the sense that even though the magnetic moments on different sites are unequal, the total magnetic moment of the unit-cell is zero. Such spin polarization in antiferromagnetic materials can be interesting for spintronics applications as they can exhibit spin Hall effect [33–35].

In order to gain insights into the origin of these electronic bands, we have calculated the site projected band structure for each lattice site and the same is presented in the figure 5. However, to illustrate the difference in the electronic structure of the metallic and gaped phases, we have presented the projected bands of only the PCO+NM and PCO+SS CFiM phases. The projected bands of the remaining three phases namely, FCO+NM,

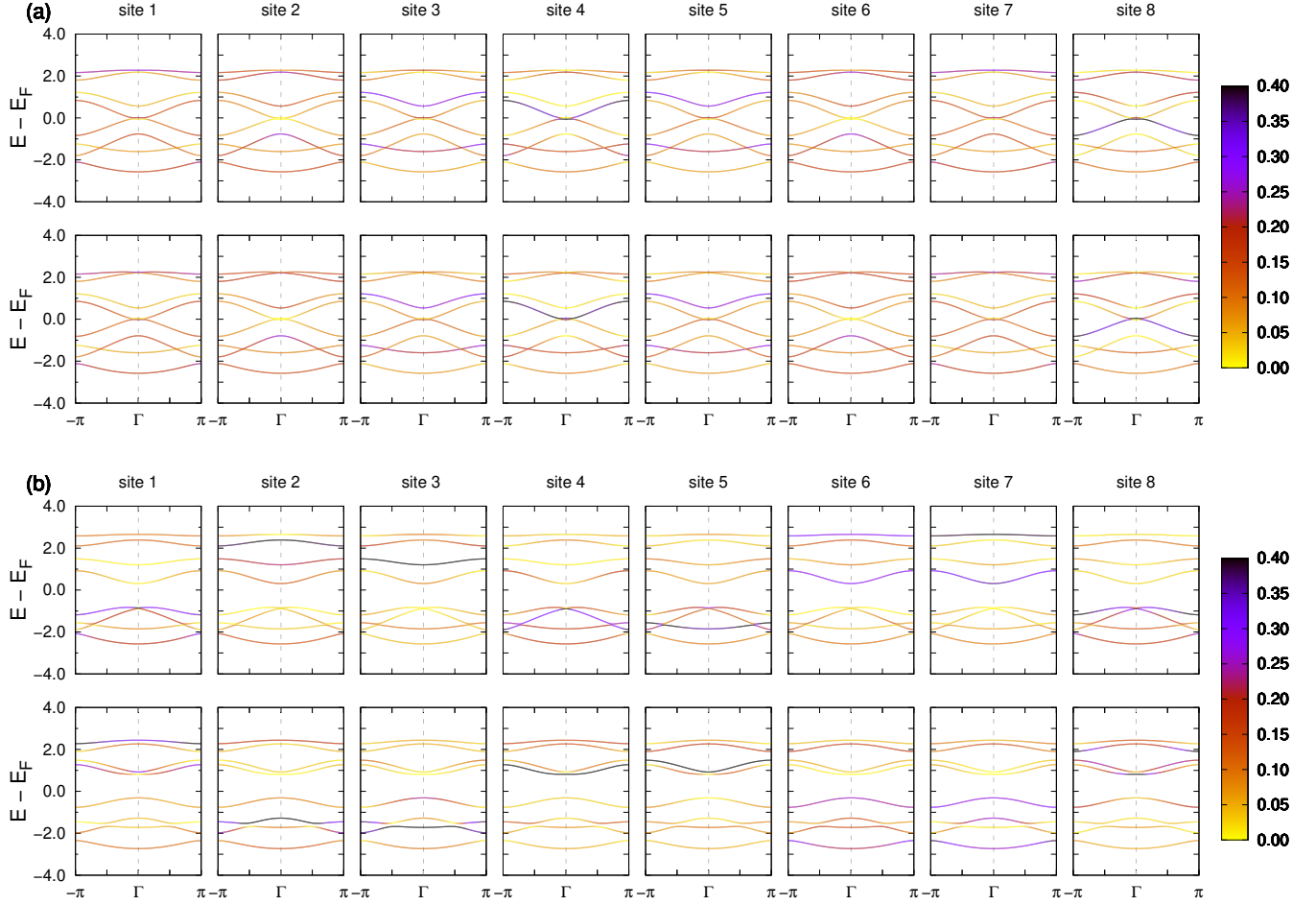


FIG. 5: Site projected electronic band structure of the (a) PCO+NM and (b) PCO+SS CFiM phases from  $k = -\pi$  to  $+\pi$ . The Fermi level is fixed at 0 eV. The top and bottom panels in (a) and (b) correspond to the up- and down-spin channels. The color scale on the right represents the weight or contribution of the particular site for a given band at different  $k$ -points. For example a band with black color represents maximum contribution by the site.

PCO+PAFM and PCO+SDW have been shown in the supporting information file. The contributions of different sites in the up- and down-spin channels are shown separately in the top and bottom rows respectively. First, we will discuss the projected band structure of the PCO+NM phase which is shown in figure 5 (a). In this phase the  $\sigma$ ,  $\mathcal{P}$  and  $\sigma\mathcal{P}$  symmetries are preserved in the ground state. This results in identical band structures for sites 1 - 7, 2 - 6, and 3 - 5 for both the spin channels. Here, the band immediately below the Fermi level ( $E_F$ ) in the up- and down-spin channels is dominated by contributions from site 8. The band above  $E_F$  is contributed predominantly by site 4. We also notice band inversion happening at the  $\Gamma$  point, at which the weights of the site 4 is transferred to bands below the  $E_F$ . A similar observation is made in case of site 8. Furthermore, since this phase is non-magnetic, the up- and down-spin bands and their contributions of each and every sites are identical, due to the conservation of  $\mathcal{P}$  symmetry. We also

notice that there is a spin inversion plus band inversion symmetry between sites 4 and 8. For instance, the up-spin band above  $E_F$  for site 4 is similar to the down-spin band below  $E_F$  for site 8 and vice-versa.

We now discuss the band structure of the PCO+SS CFiM phase. It should be recalled that the ground state of PCO+CFiM phase is degenerate, with CFiM1 and CFiM2 magnetic configurations. The CFiM1 and CFiM2 magnetic states are related by  $\sigma\mathcal{P}$  symmetry operation. Hence, in figure 5 (b), we only present the projected band structure of the CFiM1 phase. In this phase, bands of the up- and down-spin channels are not identical, giving rise to a net spin polarization. The up-spin occupied bands are mainly contributed by sites 1, 4, 5 and 8, while the sites 2, 3, 6 and 7 contribute via the down-spin channel, due to the CFiM1 type AFM interaction. It should be noted that the CFiM1 phase does not possess any symmetry and hence the contributions from different sites in up- and down-spin channels have no correspondence.

### E. Temperature dependence

We have also studied the temperature dependence of charge and spin density of the five different phases in the range  $0 \leq T \leq 0.2$  and the results are presented in figure 4. The temperatures are in units of  $t/k_B$ , where  $k_B$  is the Boltzmann's constant. Both the charge and spin densities undergo a continuous or second-order phase transition as a function of temperature. We observe that the charge and spin orderings of the PCO+PAFM and FCO+NM phases which occur at high value of  $U$  or  $V$  are quite robust, and we do not observe any transition in the temperature range that we have studied. The PCO+NM phase exhibits a gradual melting of the charge-order. The remaining two phases namely, the PCO+SDW and PCO+SS CFiM show a subtle charge-order in the entire temperature range that we have studied. The SDW phase becomes NM above  $T = 0.14$ . The SS CFiM phase also does not show any transition and hence is stable even at high temperatures. This is crucial for room temperature spintronic applications.

### F. Berry Phase

Berry phase is the quantity that describes how the global phase accumulates when the complex wave function is carried around a closed loop, in the parameter space in general. In our case, the closed loop is carried out in the reciprocal or  $\mathbf{k}$  space. Lately, the Berry phase has widely been calculated [36] on closed two-dimensional manifold, to obtain Chern number, which is an index for the topological nature of the surface  $S$ . In case of the one-dimensional systems the berry phase is also known as the Zak phase [37] which is given by,

$$\gamma = i \sum_{n=1}^{n_b} \int_C \langle u_{n\mathbf{k}} | \nabla_{\mathbf{k}} u_{n\mathbf{k}} \rangle \cdot d\mathbf{k} \quad (4)$$

In equation 4,  $|u_{n\mathbf{k}}\rangle$  is the cell periodic part of the Bloch function, and the integration is carried over a closed loop. Calculating the berry phase using the above expression is fairly straightforward, provided the phase of the Bloch function is smooth with respect to  $\mathbf{k}$ . However, in our case, since we diagonalise  $\hat{H}_{\mathbf{k}}$  at discrete values of  $\mathbf{k}$ , the wave functions at  $\mathbf{k}$  and  $\mathbf{k} + \Delta\mathbf{k}$  is not smooth, and differ by a random phase factor. Additionally, the wave function is not well defined wherever there is band degeneracy. Therefore, the calculation of the berry phase using the equation 4 can give spurious results.

Alternate ways to calculate berry phase for the single band systems have also been proposed in the literature. There, random phase between the wave functions at  $\mathbf{k}$  and  $\mathbf{k} + \Delta\mathbf{k}$  cancels out when taking the product of the bra and ket states. In this case, the Berry phase is given by, [38, 39]

$$\gamma = - \sum_n \text{Im} \ln [\langle u_{n\mathbf{k}_0} | u_{n\mathbf{k}_1} \rangle \langle u_{n\mathbf{k}_1} | u_{n\mathbf{k}_2} \rangle \langle u_{n\mathbf{k}_2} | u_{n\mathbf{k}_3} \rangle \cdots \langle u_{n\mathbf{k}_{N-1}} | e^{-\frac{2\pi i x}{a}} | u_{n\mathbf{k}_0} \rangle] \quad (5)$$

In case of bands with degeneracy at certain  $\mathbf{k}$ -points, we need to use a multi-band approach, in which case the berry phase is calculated using the relation [40] shown below.

$$\gamma = - \text{Im} \log \left( \prod_{s=0}^{M-1} \det S(\mathbf{k}_s, \mathbf{k}_{s+1}) \right) \quad (6)$$

$$S_{nn'}(\mathbf{k}_s, \mathbf{k}_{s+1}) = \langle u_{n\mathbf{k}_s} | u_{n'\mathbf{k}_{s+1}} \rangle$$

where,  $S_{nn'}(\mathbf{k}_s, \mathbf{k}_{s+1})$  is the overlap matrix. The polarization of the system in terms of the Berry phase is given by,

$$P = \frac{\gamma}{2\pi} \pmod{e}. \quad (7)$$

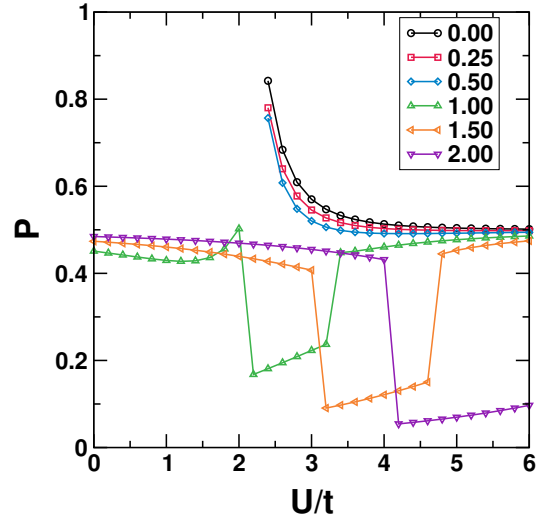


FIG. 6: Variation of Polarization as a function  $U$  for  $V = 0.0, 0.25, 0.5, 1.0, 1.5$  and  $2.0$ .

The calculated polarization,  $P$  of the system as a function of  $U$  at different  $V$  values is presented in figure 6. The system exhibits a metallic ground state for low  $U$  and  $V$  values. Valentim and coworkers have calculated the polarization of the 5/7 skewed ladder for  $U/t$  values in the range 0 - 5, in the absence of  $V$  [22]. It should be noted that our band structure calculations revealed that the system is metallic in the range  $0 \leq U \leq 2.3$  for  $V = 0$ . In the metallic state the polarization of the system is expected to be zero. Hence we have not calculated  $P$  at these values and have shown only in the phases with non-zero energy band gap. The  $V = 0$  behavior of the  $P$  vs.  $U$  plot follows the charge-order phase



transition as a function of  $U$  at a given  $V$ . For instance, when  $V = 0$ , the non-zero polarization value appears at  $U \approx 2.3$ . The value of  $P$  gradually decays to zero as we increase  $U$ . A similar behaviour is observed for  $V = 0.25$  and  $0.5$  also. When  $V$  is sufficiently large, say  $1.0$  or more, we observe multiple transitions in  $P$  as a function of  $U$ . All these transitions coincide with the charge-ordering transition of the  $5/7$  skewed ladder. For instance, in case of  $V = 1.0$  (or  $2.0$ ), we observe transitions at  $U \approx 2.0$  and  $3.3$  (or  $3.0$  and  $4.7$ ), which correspond to the FCO+NM to PCO+PAFM and PCO+PAFM to PCO+SS CFiM phase transitions respectively. In case of  $V = 2.0$ , we observe a single transition in the polarization curve, which corresponds to the FCO+NM to PCO+PAFM phase transition. The non-zero polarization in the PAFM or SS CFiM phases indicate the presence of multiferroicity in the  $5/7$  skewed ladder system.

#### IV. Discussions

Conventional antiferromagnetic materials possess net zero magnetization and hence are not useful for technological applications. This is reflected in their electronic structure as the degeneracy of the up- and down-spin bands. Rashba had proposed a momentum dependent spin splitting in materials with strong spin-orbit interactions [41]. In contrast, Šmejkal and coworkers through group theoretical studies have shown momentum dependent spin splitting in “altermagnets” possessing certain magnetic symmetry, even in the absence of relativistic effects [32, 42]. This spin splitting can enable these materials to exhibit interesting properties for technological applications like spin current, spin torque, anomalous Hall effect etc [43–45]. It should be noted that both Rashba effect and altermagnets show spin splitting in a particular momentum direction in the Brillouin zone. Recently, SS CFiM with unequal site moment but with zero net magnetization has been shown in systems like  $\text{GaFeO}_3$  [46]. Besides, SS AFM has also been proposed in  $\text{MnXN}_2$  ( $X = \text{Si, Ge, Sn}$ ) [47]. Unlike the Rashba effect or altermagnets, the SS CFiM and SS AFMs show spin splitting in the entire Brillouin zone. Even though the SS CFiM and SS AFM alleviate the stringent symmetry requirements of altermagnets, their observation in materials is very rare. In this context the spin splitting observed in our  $5/7$  skewed ladder in the PCO+SS CFiM phase gains significance. It should be noted that in this case the up- and down-spin magnetic sublattices are not connected by translation or rotational symmetry unlike the conventional antiferromagnets or altermagnets. In a conventional AFM, the combination of fractional lattice translational symmetry or spatial inversion symmetry and the time-reversal symmetry (TRS) is conserved.

But, in our  $5/7$  skewed ladder, in the ground state, the spatial inversion symmetry is broken and hence gives rise to spin splitting of the energy bands. The absence of the spatial-inversion symmetry also gives rise to net non-zero polarization in the lattice in the PCO + SS CFiM phase. The coexistence of SS and the non-zero polarisation in the PCO + SS CFiM phase makes this a SS multiferroic. SS AFMs are technologically important as they will enable us to control the magnetic property by the application of electric field. A similar observation is also made in terms of the fully charge-ordered phases FCO1 and FCO2, which are degenerate.

#### V. Conclusions

In this work, we employed an extended Hubbard model at half-filling and explored the rich landscape of electronic and magnetic ground states of a  $5/7$  skewed ladder within a mean-field framework. By tuning the on-site ( $U$ ) and inter-site ( $V$ ) Coulomb repulsions, we constructed a phase diagram that revealed multiple quantum phases in the  $U$ - $V$  parameter space. Using the unrestricted mean-field method, we identify various electronic and magnetic phases in the  $U$ - $V$  plane, by calculating the site charge and spin densities and presented the ground state phase diagram of the model. The quantum phase diagram consists of multiple competing phases including the partially and fully charge-ordered insulators, spin-density wave states, compensated ferromagnets with spin-split bands, and non-magnetic metallic regimes. Notably, we identified a unique spin-split compensated ferromagnetic phase that exhibits both spin polarisation and finite Berry phase polarisation due to the explicit broken inversion symmetry, indicative of a multiferroic behaviour. The coexistence of, spin polarisation and net electronic polarisation in this phase highlights its potential relevance to spintronics and multifunctional device applications. Our work thus offers critical insight into the interplay between charge, spin, and symmetry in low-dimensional systems, particularly those modeling realistic grain boundary geometries like the  $\{112\}$  boundary in silicon.

#### Acknowledgments

SJ and RR acknowledge Dr. Ram Janay Choudhary, UGC-DAE CSR Indore for some insightful discussions.

#### Data Availability

The data that support the findings of this article are not publicly available. The data are available from the authors upon reasonable request.

---

[1] F. Iemini, T. O. Maciel, and R. O. Vianna, *Physical Review B* **92**, 075423 (2015).

[2] M. Kumar, A. Parvej, and Z. G. Soos, *Journal of Physics:*

- Condensed Matter **27**, 316001 (2015).
- [3] T. Ogino, R. Kaneko, S. Morita, and S. Furukawa, *Phys. Rev. B* **106**, 155106 (2022).
  - [4] J. Paki, H. Terletska, S. Isakov, and E. Gull, *Physical Review B* **99**, 245146 (2019).
  - [5] P. Puddleiner, A. Kauch, K. Held, and G. Li, *Physical Review B* **100**, 075108 (2019).
  - [6] S. Sachdev, *Quantum Phase Transitions* (Cambridge University Press, 1999).
  - [7] C. Hotta and N. Furukawa, *Phys. Rev. B* **74**, 193107 (2006).
  - [8] C. Lacroix, P. Mendels, and F. Mila, *Introduction to Frustrated Magnetism* (Springer, 2011).
  - [9] S. Sarkar, J. Bhattacharya, P. Sadhukhan, D. Curcio, R. Dutt, V. K. Singh, M. Bianchi, A. Pariari, S. Roy, P. Mandal, *et al.*, *Nature Communications* **14**, 3628 (2023).
  - [10] S. Mazumdar, S. Ramasesha, R. T. Clay, and D. K. Campbell, *Physical review letters* **82**, 1522 (1999).
  - [11] M. Kumar, S. Ramasesha, and Z. Soos, *Physical Review B—Condensed Matter and Materials Physics* **79**, 035102 (2009).
  - [12] S. R. White and I. Affleck, *Phys. Rev. B* **54**, 9862 (1996).
  - [13] C. K. Majumdar and D. K. Ghosh, *J. Math. Phys.* **10**, 1388 (1969).
  - [14] D.-W. Qu, B.-B. Chen, H.-C. Jiang, Y. Wang, and W. Li, *Communications Physics* **5**, 257 (2022).
  - [15] A. K. Bera, S. Yusuf, S. K. Saha, M. Kumar, D. Voneshen, Y. Skourski, and S. A. Zvyagin, *Nature Communications* **13**, 6888 (2022).
  - [16] B. Pandey and S. K. Pati, *Phys. Rev. B* **95**, 085105 (2017).
  - [17] Z. Zhou, W. Ye, H.-G. Luo, J. Zhao, and J. Chang, *Phys. Rev. B* **108**, 195136 (2023).
  - [18] S. Das, D. Dey, M. Kumar, and S. Ramasesha, *Physical Review B* **104**, 125138 (2021).
  - [19] D. Dey, S. Das, M. Kumar, and S. Ramasesha, *Physical Review B* **101**, 195110 (2020).
  - [20] S. Thomas, S. Ramasesha, K. Hallberg, and D. Garcia, *Phys. Rev. B* **86**, 180403 (2012).
  - [21] G. Giri, Y. A. Pati, and S. Ramasesha, *The Journal of Physical Chemistry A* **123**, 5257 (2019).
  - [22] A. Valentim, D. J. García, and J. A. Plascak, *Phys. Rev. B* **105**, 174426 (2022).
  - [23] K. Kim, Z. Lee, W. Regan, C. Kisielowski, M. Crommie, and A. Zettl, *ACS nano* **5**, 2142 (2011).
  - [24] G. Giri, D. Dey, M. Kumar, S. Ramasesha, and Z. G. Soos, *Phys. Rev. B* **95**, 224408 (2017).
  - [25] S. Das, D. Dey, S. Ramasesha, and M. Kumar, *The European Physical Journal B* **95**, 147 (2022).
  - [26] S. Das, D. Dey, R. Raghunathan, Z. G. Soos, M. Kumar, and S. Ramasesha, *Physical Chemistry Chemical Physics* **26**, 36 (2024).
  - [27] S. Das, D. Dey, S. Ramasesha, and M. Kumar, *Journal of Applied Physics* **129** (2021).
  - [28] K. Hsieh, V. Kochat, T. Biswas, C. S. Tiwary, A. Mishra, G. Ramalingam, A. Jayaraman, K. Chattopadhyay, S. Raghavan, M. Jain, and A. Ghosh, *Phys. Rev. Lett.* **126**, 206803 (2021).
  - [29] R. Raghunathan, E. Johlin, and J. C. Grossman, *Nano Letters* **14**, 4943 (2014).
  - [30] Y. Claveau, B. Arnaud, and S. D. Matteo, *European Journal of Physics* **35**, 035023 (2014).
  - [31] J. Krempaský, L. Šmejkal, S. D'souza, M. Hajlaoui, G. Springholz, K. Uhlířová, F. Alarab, P. Constantinou, V. Strocov, D. Usanov, *et al.*, *Nature* **626**, 517 (2024).
  - [32] L. Šmejkal, J. Sinova, and T. Jungwirth, *Phys. Rev. X* **12**, 040501 (2022).
  - [33] T. Jungwirth, X. Marti, P. Wadley, and J. Wunderlich, *Nature nanotechnology* **11**, 231 (2016).
  - [34] N. Nagaosa, J. Sinova, S. Onoda, A. H. MacDonald, and N. P. Ong, *Rev. Mod. Phys.* **82**, 1539 (2010).
  - [35] J. Železný, H. Gao, K. Výborný, J. Zemen, J. Mašek, A. Manchon, J. Wunderlich, J. Sinova, and T. Jungwirth, *Phys. Rev. Lett.* **113**, 157201 (2014).
  - [36] R. Soni, N. Kaushal, S. Okamoto, and E. Dagotto, *Phys. Rev. B* **102**, 045105 (2020).
  - [37] J. Zak, *Phys. Rev. Lett.* **62**, 2747 (1989).
  - [38] R. Resta, *Journal of Physics: Condensed Matter* **12**, R107 (2000).
  - [39] R. Resta, *Handbook of Materials Modeling: Methods: Theory and Modeling*, 151 (2020).
  - [40] D. Vanderbilt, *Berry phases in electronic structure theory: electric polarization, orbital magnetization and topological insulators* (Cambridge University Press, 2018).
  - [41] S. Pekar and E. Rashba, *Zh. Eksperim. i Teor. Fiz.* **47** (1964).
  - [42] L. Šmejkal, J. Sinova, and T. Jungwirth, *Phys. Rev. X* **12**, 031042 (2022).
  - [43] M. Naka, S. Hayami, H. Kusunose, Y. Yanagi, Y. Motome, and H. Seo, *Nature communications* **10**, 4305 (2019).
  - [44] H. Bai, L. Han, X. Y. Feng, Y. J. Zhou, R. X. Su, Q. Wang, L. Y. Liao, W. X. Zhu, X. Z. Chen, F. Pan, X. L. Fan, and C. Song, *Phys. Rev. Lett.* **128**, 197202 (2022).
  - [45] L. Šmejkal, R. González-Hernández, T. Jungwirth, and J. Sinova, *Science advances* **6**, eaaz8809 (2020).
  - [46] J. Dong, K. Wu, M. Zhu, F. Zheng, X. Li, and J. Zhang, *arXiv preprint arXiv:2501.02914* (2025).
  - [47] L.-D. Yuan, A. B. Georgescu, and J. M. Rondinelli, *Phys. Rev. Lett.* **133**, 216701 (2024).